Enhancements in laser-generated hot-electron production via focusing cone targets at short pulse and high contrast

D. R. Rusby,[1] P. M. King,[1,2] A. Pak,[1] N. Lemos,[1] S. Kerr,[1] G. Cochran,[1] I. Pagano,[2] A. Hannasch,[2] H. Quevedo,[2] M. Spinks,[2] M. Donovan,[2] A. Link,[1] A. Kemp,[1] S. C. Wilks,[1] G. J. Williams,[1] M. J.-E. Manuel,[3] Z. Gavin,[3] A. Haid,[3] F. Albert,[1] M. Aufderheide,[1] H. Chen,[1] C. W. Siders,[1] A. Macphee,[1] and A. Mackinnon[1]

[1]*Lawrence Livermore National Laboratory, Livermore, California 94550, USA*

[2]*Department of Physics, University of Texas at Austin, Austin, Texas 78712, USA*

[3]*General Atomics, 3550 General Atomics Ave, San Diego, California 92103, USA*

(Received 14 December 2020; accepted 31 March 2021; published 14 May 2021)

We report on the increase in the accelerated electron number and energy using compound parabolic concentrator (CPC) targets from a short-pulse (∼150 fs), high-intensity ($>10^{18}$ W/cm^2), and high-contrast ($\sim 10^8$) laser-solid interaction. We report on experimental measurements using CPC targets where the hot-electron temperature is enhanced up to ∼9 times when compared to planar targets. The temperature measured from the CPC target is $\langle T_e \rangle = 4.4 \pm 1.3$ MeV. Using hydrodynamic and particle in cell simulations, we identify the primary source of this temperature enhancement is the intensity increase caused by the CPC geometry that focuses the laser, reducing the focal spot and therefore increasing the intensity of the laser-solid interaction, which is also consistent with analytic expectations for the geometrical focusing.

DOI: 10.1103/PhysRevE.103.053207

I. INTRODUCTION

Intense short-pulse laser driven production of bright high-energy sources, such as x rays [1–4], neutrons [5–7], and protons [8], has been shown to be an invaluable tool in the study of high-energy density science. However, to address some of the most challenging applications, such as x-ray radiography of high areal density objects for industrial and national security applications [1–3,9], both the yield and energy of the sources must be increased beyond what has currently been achieved by state-of-the-art high-intensity laser systems.

The yield and energy of secondary particles are typically dependent on the production of hot electrons whose distribution is commonly parameterized by $f(E) \propto A \exp(-E/T_e)$. Here A depends on the amount of laser energy that is coupled into a population of highly energetic and high-current electrons (known as hot electrons), E is the kinetic energy of the hot electrons, and T_e is their temperature. High values of both A and T_e are important for high-energy Bremsstrahlung production; one can optimize the target thickness to achieve the largest dose, but in order to create the highest-energy x rays, the highest-energy electrons achievable are desirable [10].

When interacting with a solid target, both A and T_e scale with the normalized vector potential of the laser a_0 [11–16], which is proportional to the incident intensity of the laser, $a_0 \approx 0.85\sqrt{I_{18}\lambda_\mu^2}$, where I_{18} is the intensity in units of 10^{18} W/cm^2 and λ_μ is the wavelength of the laser in microns. To control and/or enhance the yield and energy of secondary sources, much work has gone into researching methods to increase A and T_e through the use of preformed plasmas [17–19], advanced nanowires [20–23], or focusing plasma mirrors [24]. Targets with cone structures can be used to guide and/or confine the laser and plasma [25–28].

While several numerical studies have been performed on high-intensity laser-cone interactions [25,28–31], there have been relatively few experimental studies [26,27,32,33]. The target used in this study, which is of particular interest, is a compound parabolic concentrator (CPC) [34]. CPC targets are unique compared to other iterations of cones, typically straight walled cones or capillaries, as they are specifically designed to focus light into a smaller area, enabling concentration of light and utilization of the energy at the extremities of a focal spot distribution. While CPCs can be applied to larger facilities such as National Ignition Facility (NIF)-Advanced Radiographic Capability (ARC) Laser and Laser Mega-Joule (LMJ)-PETawatt Aquitaine Laser (PETAL) [35] where the facility design requires that large F-number optics must be used, they can also be used more generally at smaller laser facilities to enable access to regimes previously inaccessible.

Here we investigate the interaction between a high-intensity laser and a CPC target in a regime not previously studied, that of a short pulse (∼150 fs) and high contrast ($\sim 10^8$) where plasma expansion within the cone target is minimal. Previously presented experimental results for CPC targets [34,36] used much longer pulse durations (tens of picoseconds). For shorter laser pulses, the evolution of the plasma over the duration of the pulse is not critical to the interaction between the laser and the subcritical density plasma ($<1 \times 10^{21}$ cm^{-3}), whereas for a longer pulse the plasma can fill the CPC. For such long pulses and plasma filling, the hot electrons are accelerated superponderomotively [37,38]. Therefore, due to our relatively plasma free cone, under our experimental conditions we are able to operate the CPCs as geometric focusing devices. This allows us to focus the laser

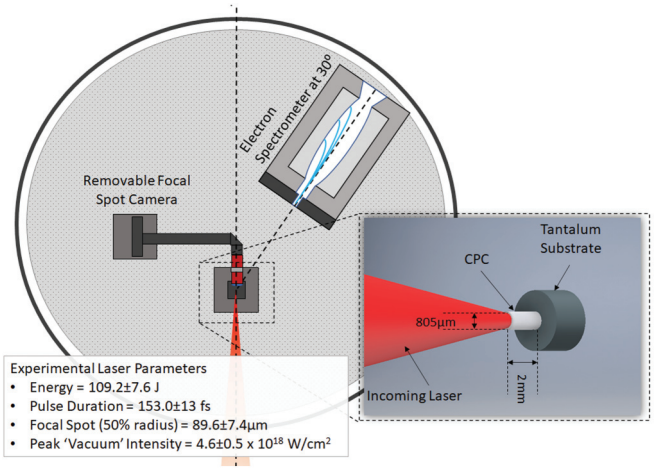

FIG. 1. A top-down schematic of the experimental setup showing the target, laser, and electron spectrometer. A 3D drawing of the CPC, tantalum substrate, and the incoming laser is also shown.

light using this microfocusing target and increase the intensity of the laser solid interaction, which leads to an enhancement in electron acceleration via the ponderomotive acceleration mechanism [14]. The enhancements in the hot-electron temperature that we observe, up to ∼9 times higher than when using a planar target geometry, are consistent with an analytical analysis of the geometric focusing. We also conclude, due to the enhancements we see in the electron distribution, that CPC targets are ideal candidates for a future target design for many areas of secondary source development where intensity or electron temperature is critical to scaling [10,39]. Finally, we show that this conclusion is consistent with two-dimensional (2D) and three-dimensional (3D) particle in cell (PIC) simulations.

II. EXPERIMENTAL CAMPAIGN

The experimental campaign was conducted on the Texas Petawatt (TPW) Laser system at the University of Texas in Austin [40]. The TPW laser is a 1.054 μm laser that delivered 109.2 ± 7.6 J on target with a pulse duration of 153.0 ± 13 fs during the experiment. We used an F/40 spherical focusing optic where the Rayleigh range is ≈14.9 mm; therefore, the size of the focal spot does not vary over the length of the 2 mm long CPC. The focal spot has a 50% enclosed energy at a radius 89.6 ± 7.4 μm and a 90% enclosed energy at 291.0 ± 16.6 μm. An example focal spot is shown in Fig. 2(a) on a logarithmic intensity scale. All values and uncertainties given are averages and standard deviations from the experimental shots. The average peak intensity is $4.6 \pm 0.5 \times 10^{18}$ W/cm^2, an a_0 of 3.9 ± 0.4. The power contrast of the TPW laser system [41] is $\sim 5 \times 10^8$ and $\sim 10^7$ at 200 and 20 ps, respectively. There is also an intrinsic pointing instability introduced from the laser. From recording the centers of 50 focal spots, this instability is 62.3 and 75.3 μm in the horizontal and vertical directions, respectively.

The original description of CPCs was given by Hinterberger and Winston in 1966 [42]. The inner surface of the CPC is a rotated parabola that is tilted about a point below the tip. Light that enters the opening aperture of the CPC within the tilted angle is transported to the tip of the CPC. The CPC targets used in this study leveraged fabrication methods utilizing two-photon polymerization (2PP). This production technique provided the means to produce many nearly identical CPCs with a tip diameter of 65 μm, which is smaller than the focal spot, and an opening aperture of 805 μm. The 2PP-printed CPCs were then attached to a 2 mm tantalum disk. The CPC here is specifically designed for the final F/40 focusing optic. The focal spot and CPC dimensions are shown in Figs. 2(a) and 2(b), respectively. The focal spot is much larger than the

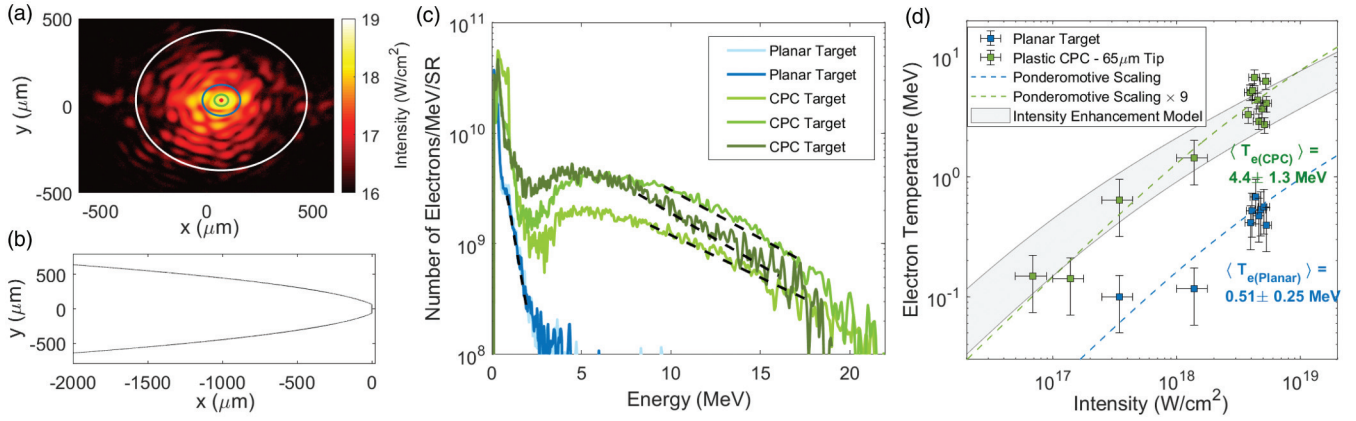

FIG. 2. (a) A sample focal spot on a logarithmic intensity scale. The outer white line represents the acceptance aperture of the CPC, and the inner green circle is the tip of the CPC. The blue circle represents the radius at which 50% of the energy is enclosed. (b) The geometry of the CPC used on the experimental campaign. The opening aperture is 805 μm, and the tip is 65 μm. (c) A sample of the electron spectra retrieved from different individual shots using the electron spectrometer on CPCs (green) or planar (blue) targets. The dashed lines represent the regions where the electron temperature is fitted. There is a clear enhancement in electron spectra when using CPC targets. (d) The hot-electron temperature from planar and CPC targets plotted against the incident laser intensity. Lower-intensity points correspond to the pulse duration scan that was performed. Both planar and CPC targets follow a ponderomotive scaling, with the CPCs having a factor of 9 enhancement. The shaded region represents the enhanced electron temperature using the ponderomotive scaling and a purely geometric focusing that increases intensity.

tip of the CPC; hence, the CPC reduces the focal spot size. Tantalum disks of the same dimensions are used as a baseline and will henceforth be referred to as planar targets. Previously, the CPCs were produced via a diamond-turned mandrel [34].

To measure the escaping electron energy distribution, an electron spectrometer [43,44] was deployed at 30° with respect to the laser axis. The signals were recorded on Fuji MS image plates for which extensive calibration material exists [45–48]. A schematic of the experimental setup is shown in Fig. 1 with the previously described laser parameters listed.

Multiple laser shots were performed on both planar and CPC targets at maximum intensity. Figure 2(c) shows a sample of electron spectra for the planar and CPC targets from multiple shots. Seven shots were preformed on the planar 2 mm tantalum targets at highest intensity. The average electron temperature from these shots was $\langle T_{e(\text{planar})}\rangle = 0.51 \pm 0.25$ MeV. Ten shots were performed on the CPC target at highest intensity. The average electron temperature from the CPCs is ∼9 times greater than the planar targets, $\langle T_{e(CPC)}\rangle = 4.4 \pm 1.3$ MeV. The uncertainty for both cases is given by the sample standard deviation. The calculated incident intensity as a function of measured electron temperature is shown in Fig. 2(d). As shown, additional measurements with lower intensities were taken which were achieved by increasing the pulse duration up to 5 ps on the CPCs and 2 ps planar targets. On-shot measurements of the pulse duration for pulses longer than 500 fs could not be made; therefore, the uncertainty becomes ±1 ps.

For high-intensity laser-solid interactions with steep density profiles, the relationship between the intensity and the electron temperature can be described using the ponderomotive scaling, where $T_{\text{pond}} = m_e c^2(\sqrt{1 + a_0^2/2} - 1)$ [14]. For the peak intensity of 4.6×10^{18} W/cm^2 the resulting ponderomotive temperature is ∼0.55 MeV, which is in close agreement with the planar targets. In Fig. 2(d), the electron temperature recorded from the CPCs, at peak intensity and with the longer pulse durations, is fitted well to a ponderomotive scaling which is increased by a factor of 9. Hence, we can initially assume that the density profile within the CPC for all pulse durations is steep.

The focusing geometry of the CPC target and the utilization of laser energy that exists in the outer region of the focal distribution are hypothesized to be the source of this enhancement of electron temperatures. Analytically, this can be considered through geometric focusing to estimate the intensity at the tip and using the ponderomotive scaling to calculate the electron temperature.

For the planar target, we assume that only regions of the focal spot where the intensity is greater than 1×10^{18} W/cm^2 are important to the generation of hot electrons as this is the intensity at which the motion of the electron within the electric field becomes relativistic. This corresponds to approximately a region with a radius $R_{\text{Focal Spot}}$ of 106 ± 17 μm and 42%±3% of the total energy $E_{>I18}$. The geometry of the CPCs will affect both of these values. The opening diameter of the CPC captures up to 92%±1% of the laser energy E_{CPC}, as shown in Fig. 2(a). We then assume that the geometry of the CPC transports all of the captured laser energy to the 32.5 μm tip R_{Tip}. Under these assumptions, the CPC is behaving as initially designed, increasing the energy and decreasing the area of the interaction. The model presented here can be used to predict the intensity for different CPC geometries and lasers. An important consideration is the previously mentioned pointing instability of the laser. If the tip of the CPC is reduced, the opening aperture is also reduced. In addition to not capturing as much of the laser, the effects of pointing instability will decrease the effectiveness of the CPC.

The total intensity enhancement can therefore be estimated by taking the ratios of the previously discussed variables: $I_{\text{enhance}} = (R^2_{\text{Focal Spot}}/R^2_{\text{Tip}})(E_{CPC}/E_{>I18})$. This model to the methodology presented by Wilson *et al.* [24] for the enhancement provided by ellipsoidal plasma mirrors. The enhancement of this optic also depends on the reflectivity of the plasma mirror under high-intensity conditions. For the CPC at peak intensity, the majority of reflections are at glancing angles and at intensities between 10^{12} and 10^{15} W/cm^2. Using HYDRA simulations [49] of the laser pedestal that interacts with the CPC walls prior to the main pulse, the temperature of the walls is calculated to be ≈3 eV and to have a scale length of ≈0.3 μm. Under these conditions, particularly with the 150 fs laser pulse where the scale length is not expected to grow vastly over the peak laser duration, we expect the reflectivity to be high.

For the average focal spot, laser energy, and pulse duration, the model yields an intensity increase of ∼36 times. Using the ponderomotive scaling, this would yield an electron temperature of ∼4.9 MeV. This calculation is performed for all record focal spots, as well as variations in the pulse duration and laser energy to provide upper and lower values for the estimated temperature enhancement; it is shown as a shaded region in Fig. 2(d). This simple model does not include field enhancements up to a factor of 4 that will occur due to constructive interference of the focused laser at the tip which can lead to further enhancements in the hot-electron temperature [50]; however, PIC simulations in the following section will take this into account.

III. SIMULATIONS

Using numerical simulations, hydrodynamics, and PIC, we can consider the role that interference and plasma play in the accelerated electron population and confirm our intensity enhancement argument. First, we conduct HYDRA simulations [49] to estimate the plasma growth prior to the peak laser arrival within the CPC. These simulations use the measured focal spot and contrast of the laser, as well as the geometry of the CPC, to accurately recreate the focusing condition prior to the pulse. A small plasma develops at the tip of the CPC that follows a double decaying exponential that can be approximated as $n(x) = n_s e^{-x/L_S} + n_c e^{-x/L_L}$, where n_s and n_c are the solid and critical densities, respectively, and L_S and L_L are the "short" and "long" scale lengths, respectively, where $L_S = 0.5$ μm and $L_L = 3$ μm.

The PIC simulations are conducted using EPOCH [51]. In order to investigate the intensity enhancement and its influence on hot-electron generation, multiple 2D and 3D simulations are conducted with varying tips sizes. Although 2D simulations are easier to perform, it is important to simulate the CPC geometry in three dimensions as there will be an

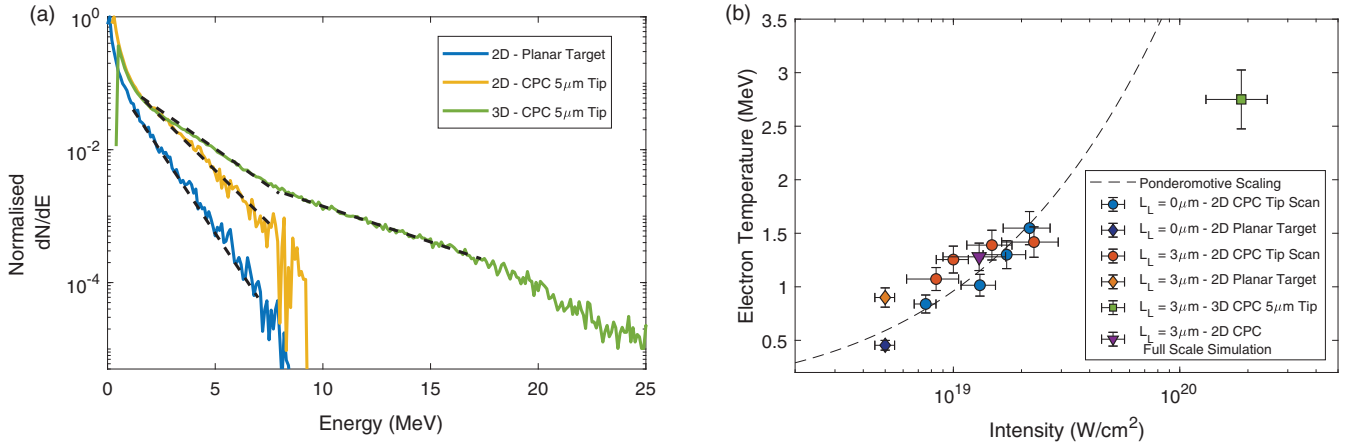

FIG. 3. (a) Hot-electron spectra from 2D planar, 2D CPC, and 3D CPC PIC simulations. The dashed lines represent temperature fits to spectra. (b) The intensity and hot-electron temperature extracted from the 2D and 3D PIC simulations. The intensity enhancements due to the focusing nature of the CPCs directly affects the temperature of the accelerated electrons.

additional focusing dimension. In two dimensions the CPC more closely resembles a wedge rather than a cone. Despite this, 2D simulation will provide some focusing, and multiple simulations can be performed to demonstrate the focusing nature of the CPCs. Following the analytical approach earlier, it is expected that smaller tips will yield higher intensities and therefore hotter electron temperatures. Due to the spatial size of the CPCs, the majority are conducted at a reduced scale of ∼6 in order to make them less computationally expensive. However, a single 2D PIC simulation was conducted at full experimental scale in order to validate the spatial reduction approach and to take into account the effect of a large focal spot on electron acceleration [36].

For the reduced-size 2D simulations, the box size is $105 \times 120\ \mu m^2$ with cell sizes of 40 nm and 40 particles per cell, whereas the 3D simulation has a reduced spatial resolution (62.5 nm) and overall box size ($90 \times 44 \times 44\ \mu m^3$) in order to make the simulation computationally viable. The spatial profile of the beam is a double Gaussian with full widths at half maximum of 20 and 65 μm with an intensity ratio of 1:0.17, determined from intensity profiles of the experimentally measured focal spot. The peak input laser intensity is 5×10^{18} W/cm^2 with a pulse duration of 150 fs full width at half maximum and a wavelength of 1.054 μm. The solid ion and electron densities are set to 50 times the critical density, and the initial electron temperature is set to 50 eV.

The electron spectra from three simulations are shown in Fig. 3(a) for a 2D planar target, 2D CPC, and 3D CPC target where the CPC simulations in two and three dimensions have a tip size of 5 μm. The CPCs show a clear increase in the observed temperature of the electrons when compared to the planar target, with the 3D simulations yielding the highest-energy electrons, a temperature of 2.75 ± 0.4 MeV. This is to be expected as the 3D simulation has the greatest intensity enhancement due to the additional focusing dimension. Intensity maps of the two CPC simulations at roughly peak intensity are shown in Figs. 4(a) and 4(b). The peak and average intensities at the tip in the 3D simulation are $\approx 4 \times 10^{20}$ W/cm^2 and $\approx 7.6 \times 10^{20}$ W/cm^2, respectively. The electron temperature for this intensity is below the ponderomotive scaling, as shown in Fig. 3(b). This is likely due to the fact that in order to simulate the system in three dimensions, the cone (as well as the laser parameters) had to be scaled down in size, thus diluting the intensification effect and reducing the transverse stochastic acceleration effects observed with a large focal spot [36].

The size of the CPC tip is varied and simulated in two dimensions to demonstrate the effect of focusing. The tips have diameters of 5, 10, 15, and 25 μm. Each case is conducted with and without $L_L = 3\ \mu$m. The case without a longer scale length represents the idealized case where geometric focusing should be the dominant effect. The intensity of the interaction is found by measuring the peak and average intensities at the approximate time that the peak laser intensity would be interacting with the surface of the target. The hot-electron temperature and intensity for the four CPC targets and planar target for the two different L_L are shown in Fig. 3(b). As the tip size is reduced, the focused intensity at the tip and extracted electron temperature increase, which closely follows the ponderomotive scaling. For both scale length cases, the CPCs have higher electron temperatures than the planar targets. However, the longer scale length planar target has a 3 times higher electron temperature compared to when there is no longer preplasma, and hence, the enhancement from planar to CPC is reduced for longer scale lengths. Although the scale length is still relatively short, as suggested by the HYDRA simulation for the condition on the experiment, the dominant enhancement process is still focusing. For much longer scale lengths ($>2L_L$), the interaction will become more similar to that shown in simulations performed by Kemp and Wilks [38] and experimental and simulations results by Williams *et al.* [36]. In these cases, the acceleration is primarily due to bulk plasma interactions and direct laser acceleration.

The full scale 2D simulation is conducted with a tip size of 65 μm with an L_L equal to 3 μm. The simulation box is $500 \times 390\ \mu m^2$ with the same spatial resolution and particles per cell as before. The temperature of the electrons was 1.28 MeV, and the peak and average intensities were 1.1×10^{19} and 8.8×10^{18} W/cm^2, respectively. These data are similar to the reduced-size data shown in Fig. 3(a); hence. we can ensure the approach of the reduced-size simulations is valid.

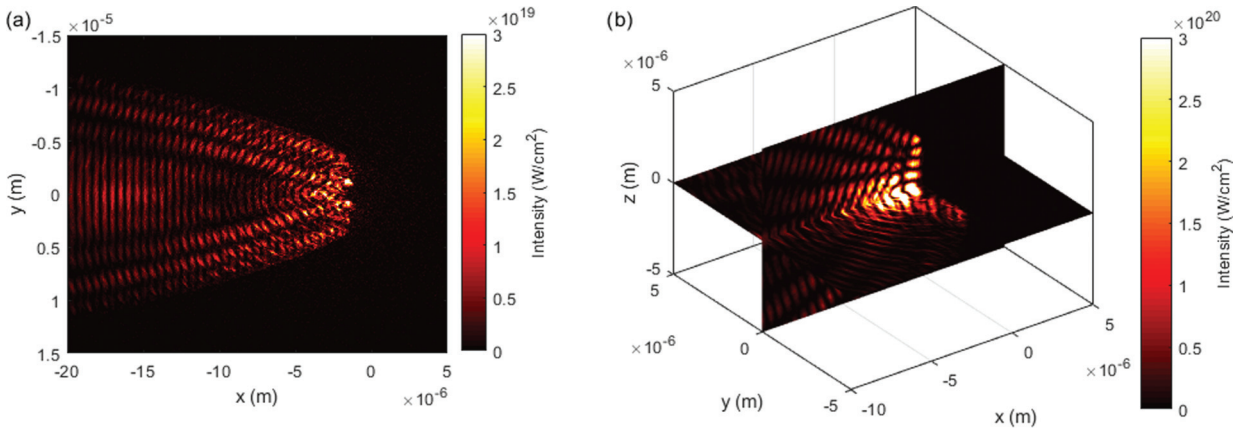

FIG. 4. Intensity profiles from the (a) 2D and (b) 3D PIC simulations respectively for the same tip size (5 μm). The intensity achieved in the 3D simulation is greater than that achieved in the 2D simulation due to the extra focusing dimension.

To understand the sensitivity of CPC focusing and hot-electron generation to experimental pointing fluctuations, additional 2D simulations were conducted. Experimentally, the pointing instability is approximately a spot width; therefore, simulations are conducted with displacements of 15 μm and 25 μm into the 5 μm tip CPC geometry. The hot-electron spectra and angular distributions of greater than 1 MeV are shown in Fig. 5. Although the electron temperature of the entire distribution has changed very little, there is a significant change in the angular distribution. This change in angular distribution is primarily caused by the laser reflecting off the wall of the CPC towards the opposite corner of the tip. This caused the interaction to be more oblique than the case where the laser has no displacement. Experimentally, the electron spectrum is measured at a single point at 30° with respect to the laser axis; in the simulations this refers to either −30° or 30°, highlighted by the arrows in the inset in Fig. 5. From the three simulations, the average hot-electron temperature at the angles of interest is $\langle T_e \rangle = 1.30 \pm 0.20$ MeV. The number of electrons at these angles also varies by a factor of ∼3. The changes in the simulated numbers of electrons, angular distribution, and temperature induced by mispointing could be a source of the shot to shot variations observed in the experimentally measured electrons we observe on our spectrometer, as shown in Fig. 2(a).

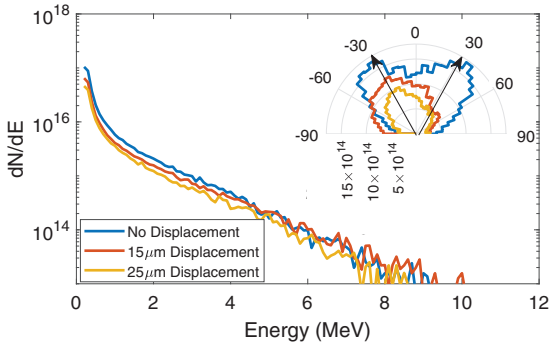

FIG. 5. Electron spectra produced when the laser is pointed in the middle and with 15 and 25 μm displacement in a 2D PIC simulation. The inset shows the change in angular distribution of electrons with energies greater than 1 MeV. The arrows represent the directions of the experimental detection of the electron spectrum.

We have experimentally demonstrated the capability of focusing cylindrical parabolic concentrator targets that have significantly increased the production of MeV electrons compared to interactions with planar targets.

Due to the high-contrast and short-pulse nature of the Texas laser pulse, we find from HYDRA simulations that the electron density gradient is steep at the target surface, and thus, we can assume that ponderomotive acceleration is the primary mechanism of acceleration. Therefore, the increase in the intensity due to the focusing of the CPC directly causes increases in the temperature of the electrons. The ∼9 times temperature enhancement observed between the planar and CPC targets here is consistent with an analytical analysis of geometric enhancement of the laser intensity at the tip of the CPC. This enhancement is higher than that observed by Macphee *et al.* [34] and Williams *et al.* [36]. This is primarily due to the laser conditions that form a plasma on the planar target surface and within the CPC, changing the electron acceleration mechanism. This interpretation is supported by detailed 2D and 3D PIC simulations of the laser plasma interaction which were largely consistent with enhanced focusing at the cone tip. The increase in the generation of hot electrons, both number and temperature, is significant as this is a critical requirement for the development of bright secondary x-ray sources for radiography and other applications. A future publication containing a full analysis of the enhancements of the x-ray generation measured in this experiment will be published at a later date [52].

ACKNOWLEDGMENTS

The authors would like to thank the facility staff at the Texas Petawatt Facility for their help conducting the experiment. This work was supported by the DOE Office of Science, Fusion Energy Sciences, under Contract No. DE-SC0019167, the LaserNetUS initiative at Texas Petawatt. This work was performed under the auspices of the U.S. Department of Energy by Lawrence Livermore National Laboratory under

Contract No. DE-AC52-07NA27344 and funded by the LLNL LDRD program under tracking code 19-SI-002 and NNSA Contract No. DE-NA0001808 for target support from General Atomic. Release under the IM:LLNL-JRNL-813462.

[1] C. Courtois *et al.*, Phys. Plasmas **18**, 023101 (2011).
[2] C. M. Brenner, S. R. Mirfayzi, D. R. Rusby, C. Armstrong, A. Alejo, L. A. Wilson, R. Clarke, H. Ahmed, N. M. Butler, D. Haddock, A. Higginson, A. McClymont, C. Murphy, M. Notley, P. Oliver, R. Allott, C. Hernandez-Gomez, S. Kar, P. McKenna, and D. Neely, Plasma Phys. Controlled Fusion **58**, 014039 (2015).
[3] D. R. Rusby, C. M. Brenner, C. Armstrong, L. A. Wilson, R. Clarke, A. Alejo, H. Ahmed, N. M. H. Butler, D. Haddock, A. Higginson, A. McClymont, S. R. Mirfayzi, C. Murphy, M. Notley, P. Oliver, R. Allott, C. Hernandez-Gomez, S. Kar, P. McKenna, and D. Neely, Proc. SPIE **9992**, 99920E (2016).
[4] H. Sawada, C. Salinas, F. N. Beg, H. Chen, A. J. Link, H. S. McLean, P. K. Patel, Y. Ping, and J. Williams, Plasma Phys. Control. Fusion **62**, 065001 (2020).
[5] N. Guler *et al.*, J. Appl. Phys. **120**, 154901 (2016).
[6] S. R. Mirfayzi, H. Ahmed, D. Doria, A. Alejo, S. Ansell, R. J. Clarke, B. Gonzales, P. Hadjisolomou, R. Heathcote, T. Hodge, P. Martin, D. Raspino, E. Schooneveld, A. Yogo, P. Mckenna, and N. J. Rhodes, Appl. Phys. Lett. **116**, 174102 (2020).
[7] I. Pomerantz, E. McCary, A. R. Meadows, A. Arefiev, A. C. Bernstein, C. Chester, J. Cortez, M. E. Donovan, G. Dyer, E. W. Gaul, D. Hamilton, D. Kuk, A. C. Lestrade, C. Wang, T. Ditmire, and B. M. Hegelich, Phys. Rev. Lett. **113**, 184801 (2014).
[8] H. Daido, M. Nishiuchi, and A. S. Pirozhkov, Rep. Prog. Phys. **75**, 056401 (2012).
[9] C. Jones *et al.*, J. Hazard. Mater. **318**, 694 (2016).
[10] A. Compant La Fontaine, J. Phys. D **47**, 325201 (2014).
[11] J. R. Davies, Plasma Phys. Controlled Fusion **51**, 014006 (2009).
[12] R. J. Gray, R. Wilson, M. King, S. D. R. Williamson, R. J. Dance, C. Armstrong, C. Brabetz, F. Wagner, B. Zielbauer, V. Bagnoud, D. Neely, and P. Mckenna, New J. Phys. **20**, 033021 (2018).
[13] Y. Ping, R. Shepherd, B. F. Lasinski, M. Tabak, H. Chen, H. K. Chung, K. B. Fournier, S. B. Hansen, A. Kemp, D. A. Liedahl, K. Widmann, S. C. Wilks, W. Rozmus, and M. Sherlock, Phys. Rev. Lett. **100**, 085004 (2008).
[14] S. C. Wilks and W. L. Kruer, IEEE J. Quantum Electron. **33**, 1954 (1997).
[15] F. N. Beg, A. R. Bell, A. E. Dangor, C. N. Danson, A. P. Fews, M. E. Glinsky, B. A. Hammel, P. Lee, P. A. Norreys, and M. Tatarakis, Phys. Plasmas **4**, 447 (1997).
[16] M. G. Haines, M. S. Wei, F. N. Beg, and R. B. Stephens, Phys. Rev. Lett. **102**, 045008 (2009).
[17] O. Culfa *et al.*, Phys. Rev. E **93**, 043201 (2016).
[18] C. Courtois, A. Compant La Fontaine, O. Landoas, G. Lidove, V. Méot, P. Morel, R. Nuter, E. Lefebvre, A. Boscheron, J. Grenier, M. M. Aléonard, M. Gerbaux, F. Gobet, F. Hannachi, G. Malka, J. N. Scheurer, and M. Tarisien, Phys. Plasmas **16**, 013105 (2009).
[19] M. I. K. Santala, M. Zepf, I. Watts, F. N. Beg, E. Clark, M. Tatarakis, K. Krushelnick, A. E. Dangor, T. McCanny, I. Spencer, R. P. Singhal, K. W. D. Ledingham, S. C. Wilks, A. C. Machacek, J. S. Wark, R. Allott, R. J. Clarke, and P. A. Norreys, Phys. Rev. Lett. **84**, 1459 (2000).
[20] S. Jiang, A. G. Krygier, D. W. Schumacher, K. U. Akli, and R. R. Freeman, Eur. Phys. J. D **68**, 283 (2014).
[21] S. Jiang, A. G. Krygier, D. W. Schumacher, K. U. Akli, and R. R. Freeman, Phys. Rev. E **89**, 013106 (2014).
[22] S. Jiang, L. L. Ji, H. Audesirk, K. M. George, J. Snyder, A. Krygier, P. Poole, C. Willis, R. Daskalova, E. Chowdhury, N. S. Lewis, D. W. Schumacher, A. Pukhov, R. R. Freeman, and K. U. Akli, Phys. Rev. Lett. **116**, 085002 (2016).
[23] T. Ebert, N. W. Neumann, L. N. K. Döhl, J. Jarrett, C. Baird, R. Heathcote, M. Hesse, A. Hughes, P. Mckenna, D. Neely, D. Rusby, G. Schaumann, C. Spindloe, A. Tebartz, N. Woolsey, and M. Roth, Phys. Plasmas **27**, 043106 (2020).
[24] R. Wilson, M. King, R. J. Gray, D. C. Carroll, R. J. Dance, C. Armstrong, S. J. Hawkes, R. J. Clarke, D. J. Robertson, D. Neely, and P. McKenna, Phys. Plasmas **23**, 033106 (2016).
[25] Y. Sentoku, K. Mima, H. Ruhl, Y. Toyama, R. Kodama, and T. E. Cowan, Phys. Plasmas **11**, 3083 (2004).
[26] K. A. Tanaka *et al.*, Phys. Plasmas **10**, 1925 (2003).
[27] S. A. Gaillard, T. Kluge, K. A. Flippo, M. Bussmann, B. Gall, T. Lockard, M. Geissel, D. T. Offermann, M. Schollmeier, Y. Sentoku, and T. E. Cowan, Phys. Plasmas **18**, 056710 (2011).
[28] T. Kluge, S. A. Gaillard, K. A. Flippo, T. Burris-Mog, W. Enghardt, B. Gall, M. Geissel, A. Helm, S. D. Kraft, T. Lockard, J. Metzkes, D. T. Offermann, M. Schollmeier, U. Schramm, K. Zeil, M. Bussmann, and T. E. Cowan, New J. Phys. **14**, 023038 (2012).
[29] S. Yang, W. Zhou, J. Jiao, Z. Zhang, L. Cao, Y. Gu, and B. Zhang, Phys. Plasmas **24**, 033106 (2017).
[30] L.-X. Hu, T.-P. Yu, F.-Q. Shao, D.-B. Zou, and Y. Yin, Phys. Plasmas **22**, 033104 (2015).
[31] R. Kodama, K. Mima, K. A. Tanaka, Y. Kitagawa, H. Fujita, K. Takahashi, A. Sunahara, K. Fujita, H. Habara, T. Jitsuno, Y. Sentoku, T. Matsushita, T. Miyakoshi, N. Miyanaga, T. Norimatsu, H. Setoguchi, T. Sonomoto, M. Tanpo, Y. Toyama, and T. Yamanaka, Phys. Plasmas **8**, 2268 (2001).
[32] N. Renard-Le Galloudec, E. d'Humières, B. I. Cho, J. Osterholz, Y. Sentoku, and T. Ditmire, Phys. Rev. Lett. **102**, 205003 (2009).
[33] A. G. MacPhee *et al.*, Phys. Rev. Lett. **104**, 055002 (2010).
[34] A. G. MacPhee, D. Alessi, H. Chen, G. Cochran, M. R. Hermann, D. H. Kalantar, A. J. Kemp, S. M. Kerr, A. J. Link, T. Ma, A. J. Mackinnon, D. A. Mariscal, D. Schlossberg, R. Tommasini, S. Vonhof, C. C. Widmayer, S. C. Wilks, G. Jackson Williams, W. H. Williams, and K. Youngblood, Optica **7**, 129 (2020).
[35] A. Casner, T. Caillaud, S. Darbon, A. Duval, I. Thfouin, J. P. Jadaud, J. P. LeBreton, C. Reverdin, B. Rosse, R. Rosch, N. Blanchot, B. Villette, R. Wrobel, and J. L. Miquel, High Energy Density Phys. **17**, 2 (2015).
[36] G. J. Williams *et al.*, Phys. Rev. E **103**, L031201 (2021).

[37] A. P. Robinson, A. V. Arefiev, and D. Neely, Phys. Rev. Lett. **111**, 065002 (2013).
[38] A. J. Kemp and S. C. Wilks, Phys. Plasmas **27**, 103106 (2020).
[39] J. Fuchs, P. Antici, E. D'Humières, E. Lefebvre, M. Borghesi, E. Brambrink, C. A. Cecchetti, M. Kaluza, V. Malka, M. Manclossi, S. Meyroneinc, P. Mora, J. Schreiber, T. Toncian, H. Pépin, and P. Audebert, Nat. Phys. **2**, 48 (2006).
[40] M. Martinez, W. Bang, G. Dyer, X. Wang, E. Gaul, T. Borger, M. Ringuette, M. Spinks, H. Quevedo, A. Bernstein, M. Donovan, and T. Ditmire, in *Advanced Accelerator Concepts: 15th Advanced Accelerator Concepts Workshop*, AIP Conf. Proc. No. 1507 (AIP, Melville, NY, 2012), p. 874.
[41] E. Gaul, T. Toncian, M. Martinez, J. Gordon, M. Spinks, G. Dyer, N. Truong, C. Wagner, G. Tiwari, M. E. Donovan, T. Ditmire, and B. M. Hegelich, J. Phys.: Conf. Ser. **717**, 012092 (2016).
[42] H. Hinterberger and R. Winston, Rev. Sci. Instrum. **37**, 1094 (1966).
[43] H. Chen, A. J. Link, R. Van Maren, P. K. Patel, R. Shepherd, S. C. Wilks, and P. Beiersdorfer, Rev. Sci. Instrum. **79**, 3 (2008).
[44] D. Mariscal, G. J. Williams, H. Chen, S. Ayers, N. Lemos, S. Kerr, and T. Ma, Rev. Sci. Instrum. **89**, 10I145 (2018).
[45] A. L. Meadowcroft, C. D. Bentley, and E. N. Stott, Rev. Sci. Instrum. **79**, 113102 (2008).
[46] T. Bonnet, M. Comet, D. Denis-Petit, F. Gobet, F. Hannachi, M. Tarisien, M. Versteegen, and M. M. Aléonard, Rev. Sci. Instrum. **84**, 103510 (2013).
[47] B. R. Maddox, H. S. Park, B. A. Remington, N. Izumi, S. Chen, C. Chen, G. Kimminau, Z. Ali, M. J. Haugh, and Q. Ma, Rev. Sci. Instrum. **82**, 023111 (2011).
[48] G. J. Williams, B. R. Maddox, H. Chen, S. Kojima, and M. Millecchia, Rev. Sci. Instrum. **85**, 11E604 (2014).
[49] M. M. Marinak, S. G. Glendinning, R. J. Wallace, B. A. Remington, K. S. Budil, S. W. Haan, R. E. Tipton, and J. D. Kilkenny, Phys. Rev. Lett. **80**, 4426 (1998).
[50] J. Ferri, E. Siminos, and T. Fülöp, Commun. Phys. **2**, 40 (2019).
[51] T. D. Arber, K. Bennett, C. S. Brady, A. Lawrence-Douglas, M. G. Ramsay, N. J. Sircombe, P. Gillies, R. G. Evans, H. Schmitz, A. R. Bell, and C. P. Ridgers, Plasma Phys. Controlled Fusion **57**, 113001 (2015).
[52] P. M. King *et al.* (private communication).